



## Simultaneous identification of a plasmaspheric plume by a ground magnetometer pair and IMAGE Extreme Ultraviolet Imager

S. Abe,<sup>1,2</sup> H. Kawano,<sup>2,3</sup> J. Goldstein,<sup>4</sup> S. Ohtani,<sup>5</sup> S. I. Solovyev,<sup>6</sup> D. G. Baishev,<sup>6</sup>  
and K. Yumoto<sup>2,3</sup>

Received 7 February 2006; revised 1 August 2006; accepted 18 August 2006; published 1 November 2006.

[1] We have compared two quantities which were simultaneously observed by two different instruments at the same point of the plasmaspheric plume. One quantity is the field-line eigenfrequency, which was obtained by applying the dual-station H-component power ratio method to geomagnetic data obtained from two ground magnetometers (at Tixie and Chokurdakh) of the Circum-pacific Magnetometer Network (CPMN). The other is the He<sup>+</sup> column abundance obtained by the IMAGE satellite Extreme Ultraviolet Imager (IMAGE/EUV). We used the EUV He<sup>+</sup> column abundance data mapped to the equatorial footpoint of the field-line whose eigenfrequency we obtained from the ground data. The mapped EUV He<sup>+</sup> column abundance is roughly proportional to the equatorial density of He<sup>+</sup>. The result of the IMAGE/EUV analysis showed an increase-then-decrease pattern of the He<sup>+</sup> column abundance. On the other hand, as a result of analyzing the simultaneously observed ground magnetometer data, we found that the eigenfrequency showed a coherent decrease-then-increase pattern. Since this pattern takes place if the equatorial plasma density along the field line increased and then decreased, these two results are qualitatively consistent. In addition, the H-power ratio showed an offset when either Tixie or Chokurdakh (these stations are longitudinally separated) stayed inside the plume. This feature can be explained if the overall ULF wave power was weaker in the plume than in the surrounding trough. With the above findings, this paper is the first to identify a plume from both the spacecraft image and the ground magnetometer ULF waves.

**Citation:** Abe, S., H. Kawano, J. Goldstein, S. Ohtani, S. I. Solovyev, D. G. Baishev, and K. Yumoto (2006), Simultaneous identification of a plasmaspheric plume by a ground magnetometer pair and IMAGE Extreme Ultraviolet Imager, *J. Geophys. Res.*, *111*, A11202, doi:10.1029/2006JA011653.

### 1. Introduction

[2] The plasmasphere is the region filled with high-density cold plasma of ionospheric origin and has the radius of several Earth radii. In its boundary layer, called the plasmopause, the plasma density drastically decreases with increasing  $L$ , and thus the Alfvén velocity,  $V_A$ , drastically increases with increasing  $L$  [e.g., Taylor *et al.*, 1958]. The shape of the plasmopause is longitudinally asymmetric, having larger radius in the afternoon sector than in the

morning sector [e.g., Carpenter, 1966]. The shape of the plasmasphere changes depending on the geomagnetic activity. Thus the shape of the plasmasphere, including its radius and the order of asymmetry, could be used as measures of the geomagnetic activity. In the past, features of the plasmasphere were studied by using data from satellites [e.g., Chappell, 1972] and whistler waves [e.g., Carpenter, 1970]. Another way to diagnose the plasmasphere, which is frequently used in recent years, is to use ground-observed ultra low frequency (ULF) waves generated by the field line resonance (FLR) [e.g., Southwood, 1974].

[3] FLR is widely accepted as one of the generation mechanisms of Pc 3–5 ULF waves (period: 10–600 s). A brief summary of the FLR mechanism is that a compressional surface wave mode couples to an Alfvén mode eigenoscillation of a geomagnetic field line. One technique to determine the frequency of the field line eigenoscillation in the magnetosphere is the dual-station H-component power ratio method (the same as “the amplitude gradient method”) [Baransky *et al.*, 1985]. This method uses two stations

<sup>1</sup>Venture Business Laboratory, Kyushu University, Fukuoka, Japan.

<sup>2</sup>Space Environment Research Center, Kyushu University, Fukuoka, Japan.

<sup>3</sup>Faculty of Science, Kyushu University, Fukuoka, Japan.

<sup>4</sup>Space Science and Engineering Division, Southwest Research Institute, San Antonio, Texas, USA.

<sup>5</sup>Johns Hopkins University Applied Physics Laboratory, Laurel, Maryland, USA.

<sup>6</sup>Institute of Cosmophysical Research and Aeronomy, Moscow, Russia.

**Table 1.** Locations of the Two Stations Used for Analysis<sup>a</sup>

Station Name	Abbreviation	GLat, deg	GLon, deg	MLat, deg	MLon, deg	$L$
Tixie	TIK	71.59	128.78	65.65	196.90	5.98
Chokurdakh	CHD	70.62	147.89	64.66	212.14	5.55

<sup>a</sup>Headings are station name, abbreviation, geographic latitude, geographic longitude, corrected geomagnetic latitude, corrected geomagnetic longitude, and  $L$  value.

closely separated in latitude. More details will be stated in section 2.

[4] There exists another method to diagnose the plasmasphere with ground-based instruments, which is that using total electron contents (TEC) [e.g., *Foster et al.*, 2002]. TEC, i.e., the number of all electrons along the radio-propagation path from the GPS satellite to a ground receiver, is measured by using the phase shift of the radio wave from the GPS satellite. By tomography of TEC data from simultaneously obtained radio propagation paths, one could obtain the spatial distribution of the electron/ion number density at a given time point [e.g., *Kersley et al.*, 2005]. On the other hand, if one uses a model of the distribution of the mass density along the field line (with the equatorial mass density,  $\rho_{eq}$ , as a free parameter), calculates the FLR frequency, and equalizes it to the observed FLR frequency, one could estimate  $\rho_{eq}$  and the field-line distribution of the mass density at the same point [e.g., *Schulz*, 1996]. Then, along the FLR field lines, one could obtain information on the ion species by comparing the obtained mass density with the number density (obtained by TEC) at each altitude. This is not the subject of this paper, but it would deserve to be perused in the future as a method to obtain global snapshots of the distribution of the ion species ratio from remote-sensing data (i.e., GPS/TEC data and data from ground magnetometer networks), which can be tested by in situ measurements [e.g., *Craven et al.*, 1997; *Dandouras et al.*, 2005].

[5] There also exists a method to remotely diagnose the plasmasphere from space, which is to use images of the plasmasphere taken by Extreme Ultraviolet Imager (EUV) on board the IMAGE (Imager for Magnetopause-to-Aurora Global Exploration) satellite [*Burch*, 2000]. The EUV images visualize structures of the plasmasphere, in addition to providing (line-of-sight integrated)  $\text{He}^+$  density. Details of IMAGE/EUV will be stated in section 3.

[6] In the present case study we compare the two of the three new plasmasphere analysis methods stated above. In the ground analysis part, we use one ground magnetometer pair, Tixie (TIK) and Chokurdakh (CHD), which are located at high latitudes. These two stations belong to the Circum-pacific Magnetometer Network (CPMN). Table 1 shows detailed information of these stations. In the satellite analysis part, we use EUV image data obtained by IMAGE satellite. It is important to conduct such a comparative study for the following reason. IMAGE/EUV can instantaneously observe the entire plasmasphere, but it can do so only near the apogee of IMAGE. In addition, there could be time when there will be no satellite like IMAGE to monitor the plasmasphere. On the other hand, ground magnetometers are easier to keep than satellites, and they can make continuous obser-

varations, but their spatial coverage is less complete than IMAGE/EUV. We also note that our current method by using one ground magnetometer pair can detect plasma-pause boundary layer, but it is difficult to distinguish variety of plasmaspheric features with similar sharp density gradients. It will be possible to distinguish plasmaspheric structures by using many ground magnetometer station pairs that are closely distributed, but we do not have enough stations now. Therefore it is important to use both methods and to compare the results of the two methods, which is the objective of this study.

## 2. Plasmasphere Observations by Using Ground Magnetometer Networks

[7] The dual-station H-component power ratio method is based on latitude dependence of the H-component power of the field-line eigenoscillation. The amplitude of eigenoscillation is largest at its resonant point. Figures 1, 2, and 3 illustrate this method, and they also illustrate what is expected in the results of applying this method to our data. Figure 1 shows the latitudinal profiles of the H-component power of the eigenoscillation at frequencies  $f_1$ ,  $f_2$ , and  $f_r$ :  $f_i$  ( $i = 1, 2, r$ ) is a resonant frequency at  $S_i$ . That is, the power of the Fourier component of  $H$  having frequency  $f_i$  becomes maximum at  $S_i$ . Thus if one divides the power of  $H$  at  $S_2$  by that at  $S_1$  for each frequency, it becomes minimum near  $f_1$  and becomes maximum near  $f_2$ . As a result, the ratio shows a bipolar pattern centered near  $f_r$ .

[8] The next question is if the bipolar pattern is an increase-then-decrease pattern or a decrease-then-increase

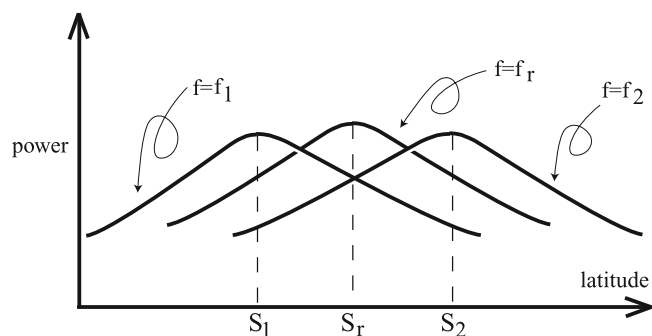


**Figure 1.** Ground-latitude profiles of the powers of waves, having different frequencies, under field line resonances (FLR). Also shown are the relative locations of ground stations  $S_1$  and  $S_2$ , and its midpoint  $S_r$ . The horizontal axis shows latitude. The vertical axis shows the power. The curve labeled “ $f = f_i$ ” shows the power of the wave having the frequency  $f_i$ , under resonance at  $S_i$ .

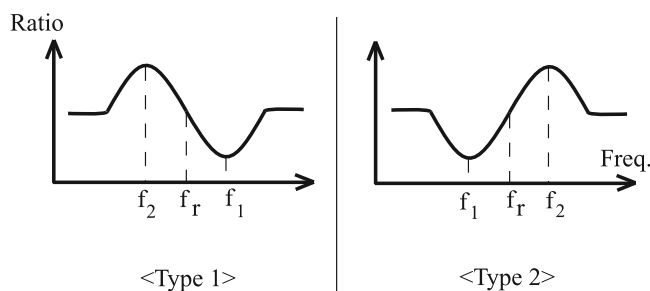


**Figure 2.** The frequency profile of the power ratio of the two stations (high latitude/low latitude). Here  $f_r$  is the resonance frequency at the midpoint of the two stations. Type 1 refers to an increase-then-decrease pattern with increasing frequency (left panel). Type 2 refers to a decrease-then-increase pattern (right panel).

pattern (with increasing frequency): Apparently, the former (called Type 1 below) occurs when  $f_1 > f_2$ , and the latter (called Type 2 below) occurs when  $f_1 < f_2$ . Type 1 (2) is illustrated in Figure 2, left (right) panel.

[9] Since  $\frac{1}{f_i} \simeq \int \frac{ds}{V_A}$ , where the integration is made along the field line running through  $S_i$ ,  $f_i$  decreases with increasing  $L$  if the field-line length increases and  $V_A$  decreases at the same time; which is usually the case in the magnetosphere. Thus  $f_1 > f_2$  is usually the case, leading to Type 1.

[10] On the other hand, if  $V_A$  drastically increases with increasing  $L$ ,  $f_i$  can increase with increasing  $L$ , resulting in  $f_1 < f_2$ , that is, Type 2. Such a situation can take place in the plasmopause layer, since the plasma density there drastically decreases with increasing  $L$ . Figure 3a illustrates the density, Figure 3b illustrates  $V_A$ , and Figure 3c illustrates and the resonance frequency  $f_{FLR}$ , as a function of  $L$ , along with field-aligned mapped locations of (assumed)  $S_1$  and  $S_2$  and corresponding  $f_1$  and  $f_2$  (Figure 3c), for quiet time magnetosphere. (During geomagnetically perturbed intervals, Type 1 and 2 can take place at different locations, as shown later in this paper.)

[11] We emphasize that in this section we described the method in terms of the latitudinal structure because many magnetospheric structures have a latitudinal gradient. However, if a magnetospheric structure has a longitudinal gradient (for example, a plume is such), a station pair with a longitudinal separation can be used for identifying such a gradient.

### 3. IMAGE Satellite and EUV

[12] The IMAGE satellite observes plasma environments around the earth. Its difference from current space satellites that make in situ observations is that IMAGE uses new technologies such as the EUV imager to grasp global features of physical phenomena. It was launched by NASA in March 2000 with the orbital period of 14.2 hours, the apogee of  $8.2 R_E$  ( $R_E$  is Earth radius) above the north pole, and the perigee of  $1.2 R_E$ .

[13] The EUV imager is one of seven scientific instruments on board the IMAGE satellite. This imager detects

the scattered emission of  $\text{He}^+$  (30.4 nm). The entire plasmasphere can be imaged by this instrument because the plasmasphere includes significant amount of  $\text{He}^+$ . The EUV intensity also serves as an indicator of the plasmaspheric density because the plasmasphere mainly consists of  $\text{H}^+$  and  $\text{He}^+$ , and the  $\text{He}^+$  density is proportional to the  $\text{H}^+$  density [Craven *et al.*, 1997].

[14] In addition, the mean free path of the photon is sufficiently long in the plasmasphere and we can detect the emission far away from its source. That is, the plasmasphere is optically thin for the scattered emission of  $\text{He}^+$ . Therefore almost all the scattered emission of  $\text{He}^+$  can be observed with EUV imager without being absorbed by surrounding  $\text{He}^+$ . Thus its brightness is proportional to the  $\text{He}^+$  column abundance. In this study we use the data of  $\text{He}^+$  column abundance calculated from the EUV brightness.

[15] The spatial resolution of EUV is about  $0.1 R_E$  in equatorial plane seen from the apogee distance, and the time resolution is about 10 minutes. Examples are shown at “The IMAGE EUV Instrument” home page (<http://>

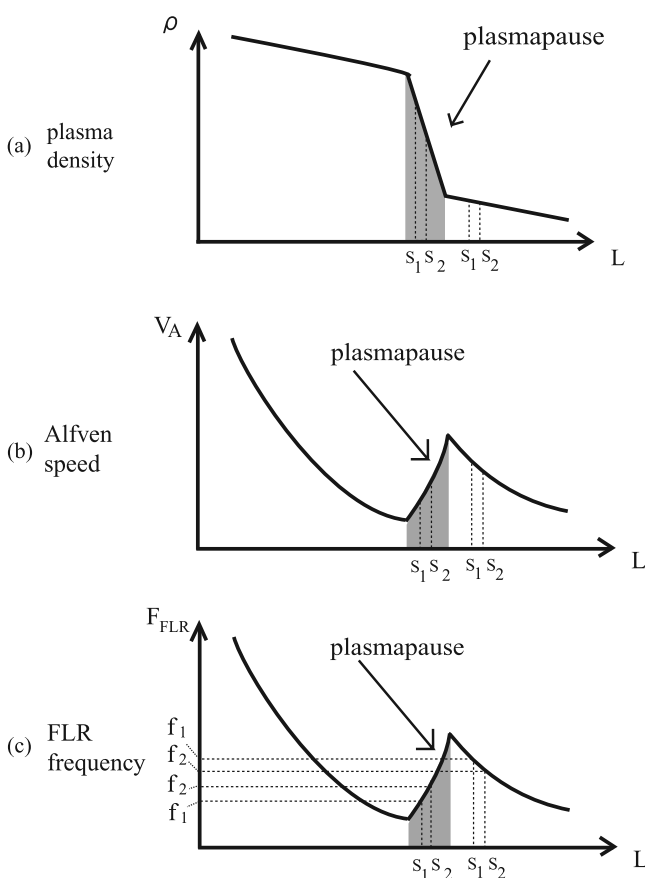


**Figure 3.** (a) The plasma density as a function of the distance from the Earth. (b) The Alfvén velocity as a function of the distance from the Earth. The plasmopause is shaded in both figures. Also shows are (assumed) field-aligned-mapped locations of two ground stations,  $S_1$  and  $S_2$ . (c) The resonant frequency as a function of the distance from the Earth.  $f_i$  shows the resonant frequency observed at  $S_i$ .

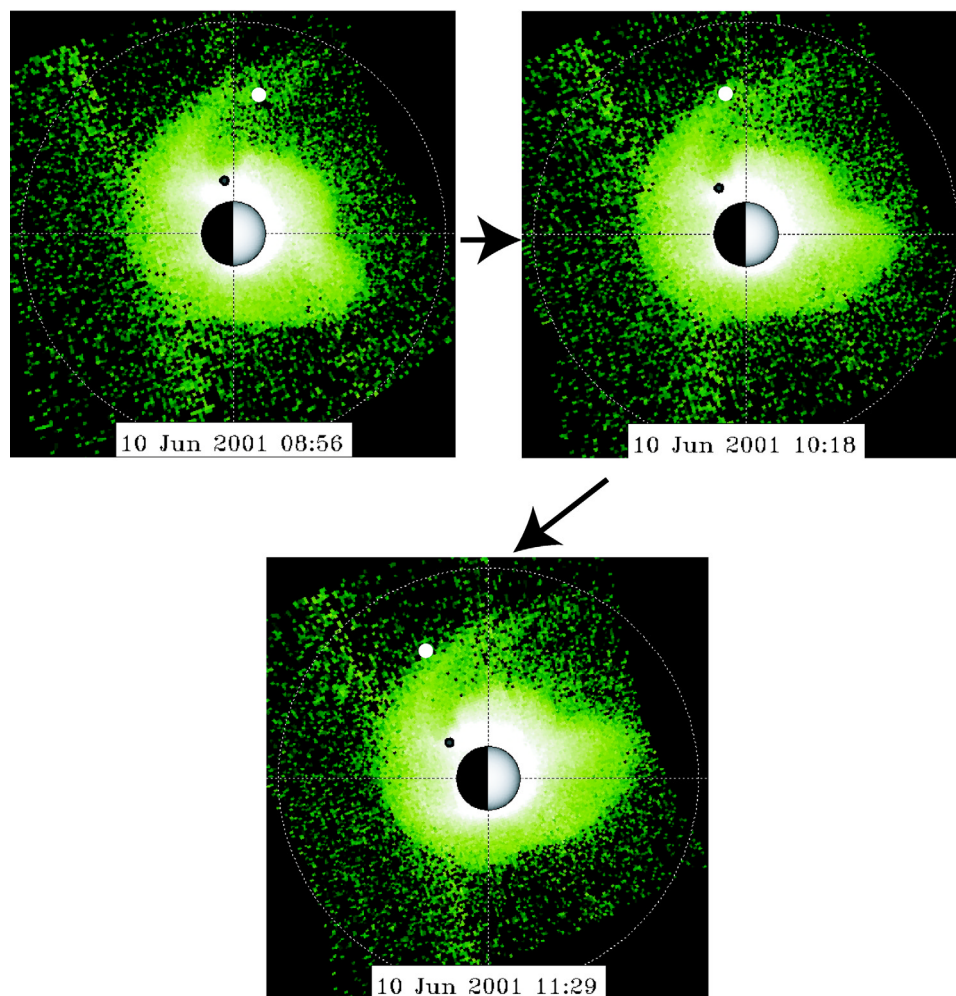


**Figure 4.** An example of the equatorial-plane mapped EUV images by using the method of *Goldstein et al.* [2003]. The white point is referred to as “mapped TIK-CHD midpoint.”

euv.lpl.arizona.edu/euv/) and in published papers [e.g., *Sandel et al.*, 1999].

#### 4. Data and Analysis Method

[16] The event we examined took place on 8–11 June 2001. When the IMAGE satellite was located near its apogee distance on 10 June, it imaged the entire plasmasphere. In addition to IMAGE/EUV, we used the ground magnetometer data observed at TIK and CHD. We applied the H-component power ratio method to these magnetometer data.

[17] As stated in section 2, by applying the H-component power ratio method to magnetometer data from adjacent two ground stations, we can estimate the density at the point where the field line running through the midpoint of the two ground stations intersects the magnetospheric equatorial plane. To obtain the EUV He<sup>+</sup> column abundance corresponding to this point and compare it with the ground-based information, we use the procedure of *Goldstein et al.* [2003] to map the EUV He<sup>+</sup> column abundance data to the magnetospheric equatorial plane; the following is a brief summary of this procedure.

[18] When the IMAGE satellite is at a polar vantage point near its apogee distance, the line of sight (LOS) is approximately perpendicular to the magnetic equatorial plane. The method assumes that the magnetic configuration is dipolar, the density decreases sharply with  $L$ -value, and that the plasmaspheric density is fairly uniform along the field line; these are all reasonable assumptions [e.g., *Goldstein et al.*, 2001; *Gallagher et al.*, 2000; *Denton and Gallagher*, 2000; *Denton et al.*, 2002; *Reinisch et al.*, 2004]. Hence the EUV He<sup>+</sup> column abundance along a LOS is roughly proportional to the density at the point where the LOS crosses its minimum  $L$ -value, and thus to the density where the field line tangent to the LOS intersects the magnetic equatorial plane (differently put, the XY plane in SM coordinates). As an example, Figure 4 shows the mapped EUV images processed by using this method for the present event. In this figure, the white point indicates the equatorial point on the field line that runs through the midpoint of TIK and CHD, which will be referred to as “mapped TIK-CHD midpoint” in the following.

[19] In this paper, we employ the above-stated zeroth-order assumptions, and use the EUV He<sup>+</sup> column

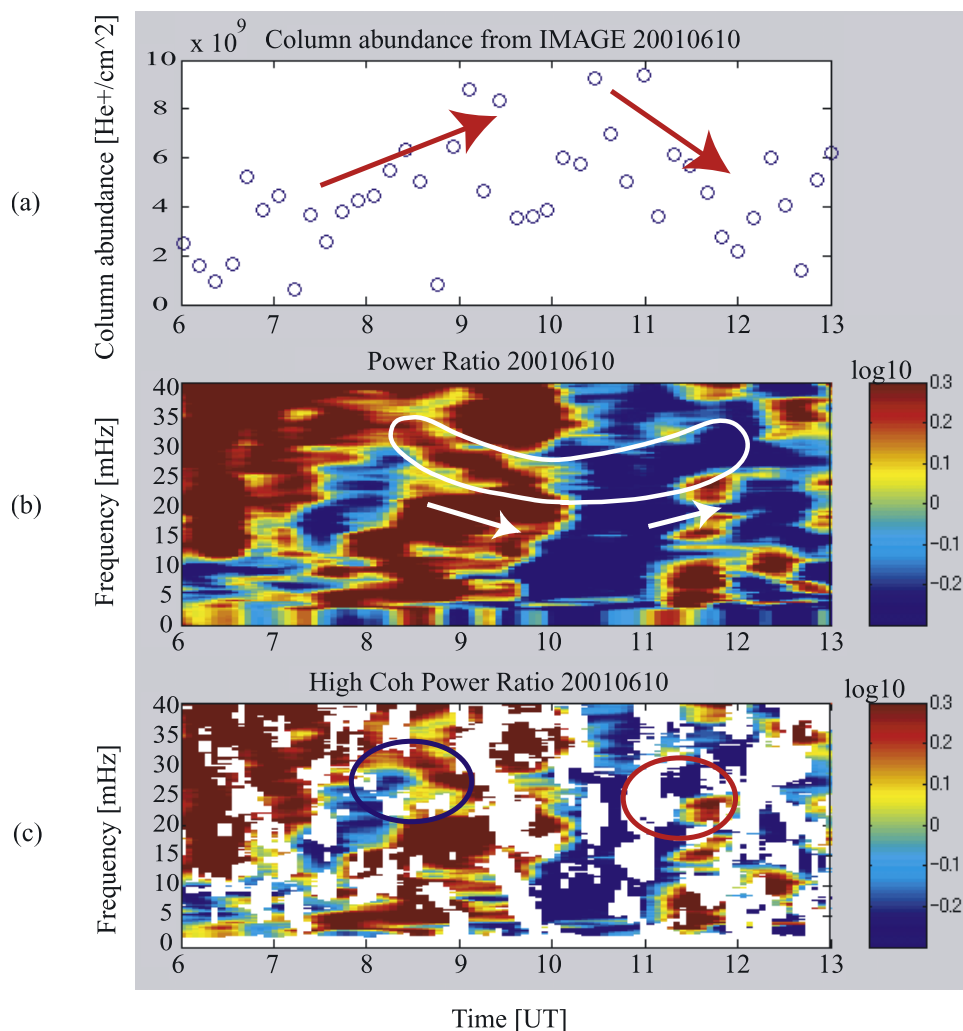


**Figure 5.** (a) The IMAGE/EUV  $\text{He}^+$  column abundance [ $\text{He}^+/\text{cm}^2$ ] corresponding to the point where the field line running through the midpoint between TIK and CHD intersects the equatorial plane. The horizontal axis shows time (UT). (b) H-component power ratio dynamic spectra (TIK/CHD). The vertical axis shows frequency [mHz], and the horizontal axis shows time (UT). (c) H-component power ratio dynamic spectra where pixels with coherence  $\leq 0.83$  are set blank.

abundance as a measure of the equatorial  $\text{He}^+$  density. The used assumptions are roughly correct as the above-cited references show. At the same time, readers are referred to *Gallagher et al.* [2005] for a caution to these assumptions.

## 5. Results of Comparisons Between the Ground Magnetometer-Based Density and the EUV $\text{He}^+$ Column Abundance

[20] Figure 5a shows the EUV  $\text{He}^+$  column abundance at the “mapped TIK-CHD midpoint”. The EUV  $\text{He}^+$  column abundance increased as the “mapped TIK-CHD midpoint” entered the plasmaspheric plume, and it decreased as the midpoint went out of the plume (see Figure 4).

[21] Figure 5b shows the dynamic spectra of the H-component power ratio (TIK over CHD). When the “mapped TIK-CHD midpoint” entered the plume (shown by the increasing trend in Figure 5a), Figure 5b shows red

colors at a wide range of frequency. On the other hand, when the “mapped TIK-CHD midpoint” went out of the plume (shown by the decreasing trend in Figure 5a), Figure 5b shows blue colors at a wide range of frequency. Figure 5c shows the dynamic spectra of the H-component power ratio between TIK and CHD where pixels with coherence  $\leq 0.83$  are set blank.

[22] In Figure 5b we can also identify a red band with decreasing frequency with time, and a blue band with increasing frequency with time as marked by a white loop and arrows. In Figure 5c we can identify the same bands, and in addition, we can see a blue (red) band just below the red (blue) band identified in Figure 5b; the paired bands are marked by red and blue circles in Figure 5c. These features will be discussed in section 6.

## 6. Discussion

[23] Here we first summarize the features we found in Figure 5.

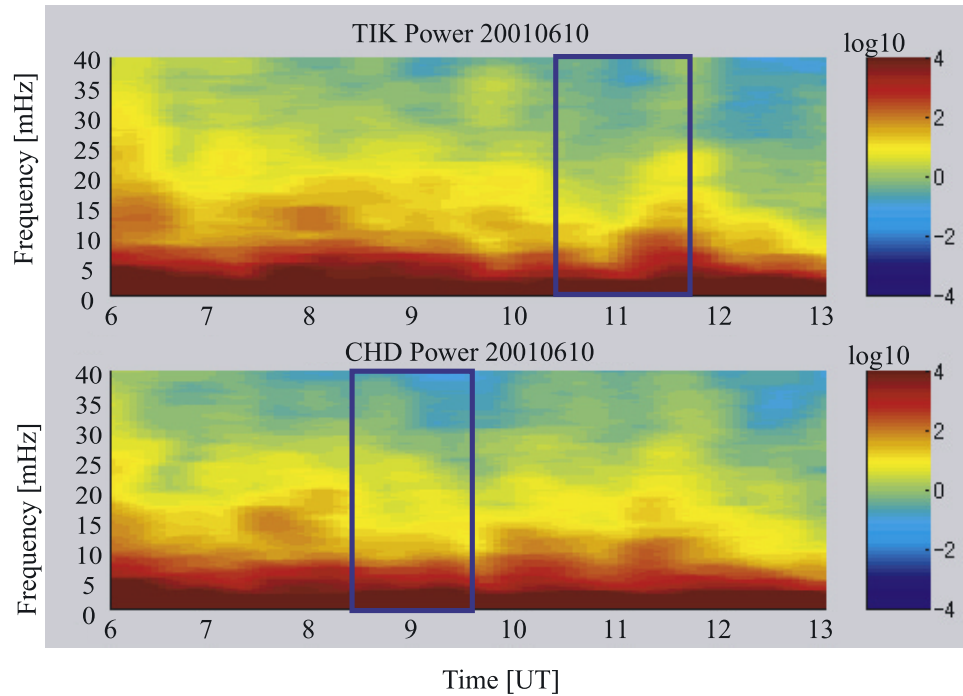


**Figure 6.** Top panel shows the power spectra of TIK. Bottom panel shows the power spectra of CHD. Blue square shows time range which decreasing power. The vertical axis shows frequency [mHz], and the horizontal axis show time (UT).

[24] 1. The EUV  $\text{He}^+$  column abundance along the LOS which intersects the magnetic equatorial footpoint of the field line running through the midpoint between TIK and CHD increased (decreased) as the field line entered (exited) the plume.

[25] 2. The background level in the power ratio (TIK/CHD) increased (decreased) when the EUV  $\text{He}^+$  column abundance increased (decreased).

[26] 3. There also existed a band of especially enhanced (reduced) power ratio (TIK/CHD) with increasing (decreasing) frequency with time when the EUV  $\text{He}^+$  column abundance increased (decreased).

[27] 4. The band of enhanced (reduced) power ratio is accompanied by a band of less-significantly reduced (enhanced) power ratio.

[28] The first feature is reasonable because the density in the plume is larger than that in the surrounding trough.

[29] The second feature can be explained as follows: Figure 6 shows the power spectral density (PSD) at each station in the same time range as Figure 5. Figure 6 reveals that the PSD at CHD was weak at 0830–0930 UT and that the PSD at TIK was weak at 1030–1140 UT (marked by blue squares in Figure 6). These intervals correspond to those when CHD (0830–0930) and TIK (1030–1140) were located in the plume: Because of the difference in longitude between TIK and CHD, only one station stayed in the plume during these intervals. The locations of CHD and TIK relative to the plume at 0830–0930 UT (1030–1140 UT) are illustrated in Figure 7a (Figure 9a). We do not have a solid explanation for the reason the power of ULF waves become weak in the plume, but we speculate that the

much heavier plasmaspheric flux tubes (heavier than in trough) are more difficult to oscillate.

[30] It is also anticipated that the Type 2 bipolar pattern was observed in the power ratio (TIK/CHD) at 0830–0930 UT, because, in the terminology of Figure 1,  $f_1$  at  $S_1 = \text{CHD}$  was lower than  $f_2$  at  $S_2 = \text{TIK}$ , where  $f_i$  is the value of  $f_{FLR}$  at  $S_i$  (see Figure 7c). Note here that the horizontal axis of Figure 7c is the local time while that of Figure 3 is L: This is because the density gradient across the plume boundary was significant not only in L but also in LT and also because TIK and CHD stations are separated more widely in LT than in L (see Table 1). In addition, because the background power was biased toward red (Figure 5b), it is expected that the maximum part of the bipolar shape in the power ratio was more significant than the minimum part when color-plotted, as illustrated in Figure 7d. Thus a red band is expected in Figure 5b, as is actually identified. This is why we interpret the red band to be caused by FLR. As a further support of this interpretation, Figure 8 shows the frequency profile of the power ratio at 0840 UT (see Figure 5c, blue circle); one can see the frequency dependence similar to that shown in Figure 7d.

[31] CHD went out of the plume while TIK entered the plume during 1030–1140 UT, as illustrated in Figure 9a. Therefore the power at CHD recovered while the power at TIK decreased. It is anticipated that the Type 1 bipolar pattern was observed in the power ratio because  $f_2$  at  $S_2 = \text{TIK}$  was smaller than  $f_1$  at  $S_1 = \text{CHD}$  (see Figure 9c). In addition, because the background power was biased toward blue (Figure 5b), it is expected that the minimum part of

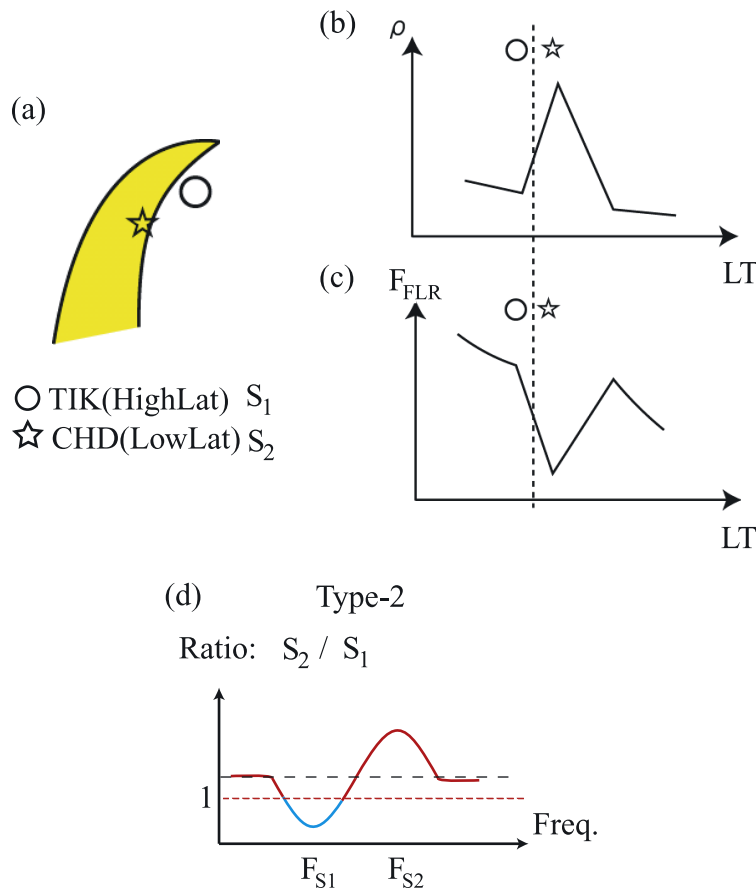


**Figure 7.** The condition during the interval 0830–0930 UT. (a) The schematic picture around the plume. (b) The plasma density around the plume as a function of the local time. (c) The resonance eigenfrequency as a function of the local time. (d) The frequency profile of the power ratio of the two stations. Black line shows a normal offset line and red line shows a biased offset line.

the bipolar shape in the power ratio was more significant than the maximum part when color-plotted, as illustrated in Figure 9d. Thus a blue band is expected in Figure 5b, as is actually identified. This is why we interpret the blue band to be caused by FLR. As a further support of this interpretation, Figure 10 shows the frequency profile of the power ratio at 1140 UT (see Figure 5c, red circle); one can see the frequency dependence similar to that shown in Figure 9d.

[32] In zeroth-order approximation, the FLR frequency is inversely proportional to the plasma density and is proportional to the field-line length. Assuming that the field-line length does not change so much while the plasma density increases and decreases, the FLR frequency increases with decreasing density, and decreases with increasing density. Thus the decrease-then-increase in the FLR frequency, identified in Figures 5b and 5c, corresponds to an increase-then-decrease in the density. On the other hand, the EUV He<sup>+</sup> column abundance (shown in Figure 5a), which is roughly proportional to the equatorial plasma density, increased (decreased) when the FLR frequency decreased (increased) (Figures 5b and 5c); thus the two data sets appear to be consistent features, which also suggests that our assumption (that the field line length

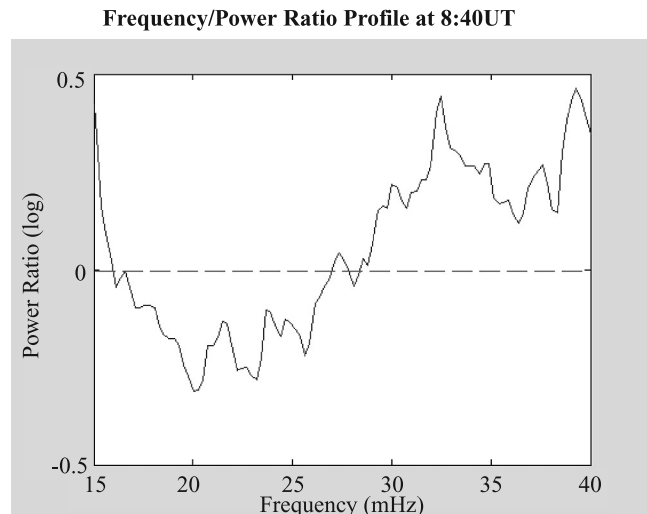


**Figure 8.** The frequency profile of the power ratio of the two stations at 0840 UT (see Figure 5c, blue circle). The dashed line shows the offset line.

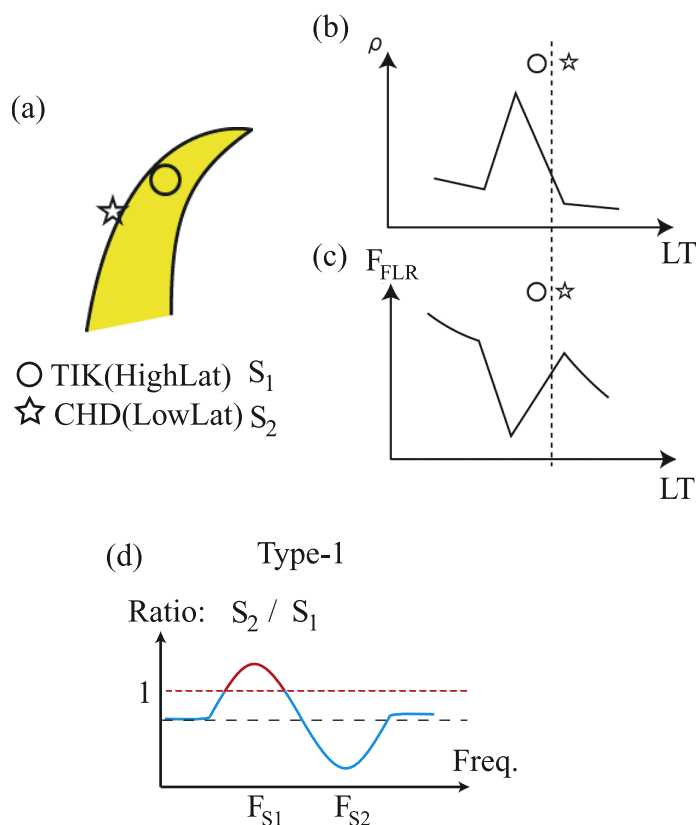


**Figure 9.** The condition during the interval 1030–1140UT, in the same format as Figure 7.

did not change so much while the plasma density increased and decreased) is reasonable for the present event.

[33] For more quantitative comparisons, it is necessary to estimate the mass density ( $\text{kg}/\text{cm}^3$ ) from the FLR frequency the actual  $\text{He}^+$  number density ( $1/\text{cm}^3$ ) from the EUV  $\text{He}^+$  column abundance. This requires some inversion techniques, and it will be the subject of a future research. The qualitative agreement we found in this study encourages such quantitative studies.

**7. Summary**

[34] For an interval when IMAGE/EUV observed a plasmaspheric plume on 10 June 2001, we have compared the two quantities at the same equatorial point in the plasmasphere: One is the IMAGE/EUV  $\text{He}^+$  column abundance, which is roughly proportional to the equatorial density of  $\text{He}^+$ . The other is the field-line eigenfrequency identified in the magnetometer data from two CPMN stations TIK and CHD, which can be used for estimating the magnetospheric plasma density. The field line running through the mid-point between TIK and CHD passed through the plume as it corotated with the Earth. By applying the dual-station H-power ratio method to TIK/CHD, we found that the field-line resonance frequency decreased and then increased, which suggests that the equatorial plasma density along the field line increased and then decreased. This pattern is the same as the density change inferred from the IMAGE/EUV observation. In addition, we found differences in the background powers at TIK and CHD when they went into

and out of the plume, which suggests that the overall ULF wave power was weaker in the plume: Because of the longitudinal separation of TIK and CHD, CHD entered (exited) the plume first before TIK entered (exited) it. In this study we identified for the first time a plume from both the space and ground magnetometer data.

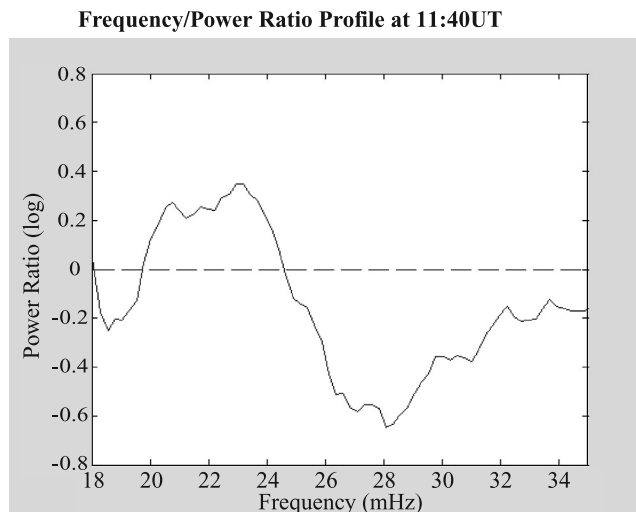


**Figure 10.** The frequency profile of the power ratio of the two stations at 1140 UT (see Figure 5c, red circle). The dashed line shows the offset line.

[35] **Acknowledgments.** The authors thank B. R. Sandel for informative discussions about the IMAGE/EUV He<sup>+</sup> column abundance. The authors' sincere thanks go to all the members of the CPMN project for their ceaseless support. The CPMN project is financially supported by the Ministry of Education, Science and Culture of Japan (and Japan Society for the Promotion of Science) as the Grants-in-Aid for Overseas Scientific Survey (05041060, 0841105, 10041122, 12373003, 15253005). Work at JHU/APL was supported by the NSF grant ATM0318173 and by the NASA grant NAG513491.

[36] Zuyin Pu thanks Dennis Gallagher and two other reviewers for their assistance in evaluating this paper.

## References

- Baransky, L. N., Y. E. Borovkov, M. B. Gokhberg, S. M. Krylov, and V. A. Troitskaya (1985), High resolution method of direct measurement of the magnetic field line eigen frequencies, *Planet. Space Sci.*, *33*, 1369.
- Burch, J. L. (2000), IMAGE mission overview, *Space Sci. Rev.*, *91*, 1–14.
- Carpenter, D. L. (1966), Whistler studies of the plasmapause in the magnetosphere: I. Temporal variations in the position of the knee and some evidence on plasma motions near the knee, *J. Geophys. Res.*, *71*, 693.
- Carpenter, D. L. (1970), Whistler evidence of the dynamic behavior of the duskside bulge in the plasmasphere, *J. Geophys. Res.*, *75*, 3837.
- Chappell, C. R. (1972), Recent satellite measurements of the morphology and dynamics of the plasmasphere, *Rev. Geophys.*, *10*, 951.
- Craven, P. D., D. L. Gallagher, and R. H. Comfort (1997), Relative concentration of He<sup>+</sup> in the inner magnetosphere as observed by the DE1 retarding ion mass spectrometer, *J. Geophys. Res.*, *102*, 2279.
- Dandouras, I., et al. (2005), Multipoint observations of ionic structures in the plasmasphere by CLUSTER-CIS and comparisons with IMAGE-EUV observations and with model simulations, in *Inner Magnetosphere Interactions: New Perspectives From Imaging*, *Geophys. Monogr. Ser.*, vol. 159, edited by J. L. Burch, M. Schulz, and H. Spence, pp. 23–53, AGU, Washington, D. C.
- Denton, R. E., and D. L. Gallagher (2000), Determining the mass density along magnetic field lines from toroidal eigenfrequencies, *J. Geophys. Res.*, *105*, 27,717–27,725.
- Denton, R. E., J. Goldstein, and J. D. Menietti (2002), Field line dependence of magnetospheric electron density, *Geophys. Res. Lett.*, *29*(24), 2205, doi:10.1029/2002GL015963.
- Foster, J. C., P. J. Erickson, A. J. Coster, J. Goldstein, and J. Rich (2002), Ionospheric signatures of plasmaspheric tails, *Geophys. Res. Lett.*, *29*(13), 1623, doi:10.1029/2002GL015067.
- Gallagher, D. L., P. D. Craven, and R. H. Comfort (2000), Global core plasma model, *J. Geophys. Res.*, *105*, 18,819–18,833.
- Gallagher, D. L., M. L. Adrian, and M. N. Liemohn (2005), Origin and evolution of deep plasmaspheric notches, *J. Geophys. Res.*, *110*, A09201, doi:10.1029/2004JA010906.
- Goldstein, J., R. E. Denton, M. K. Hudson, E. G. Miftakhova, S. L. Young, J. D. Menietti, and D. L. Gallagher (2001), Latitudinal density dependence of magnetic field lines inferred from Polar plasma wave data, *J. Geophys. Res.*, *106*, 6195.
- Goldstein, J., M. Spasojević, P. H. Reiff, B. R. Sandel, W. T. Forrester, D. L. Gallagher, and B. W. Reinisch (2003), Identifying the plasmapause in IMAGE EUV data using IMAGE RPI in situ steep density gradients, *J. Geophys. Res.*, *108*(A4), 1147, doi:10.1029/2002JA009475.
- Kersley, L., S. E. Pryse, M. H. Denton, G. Bust, E. Fremouw, J. Secan, N. Jakowski, and G. J. Bailey (2005), Radio tomographic imaging of the northern high-latitude ionosphere on a wide geographic scale, *Radio Sci.*, *40*, RS5003, doi:10.1029/2004RS003103.
- Reinisch, B. W., X. Huang, P. Song, J. L. Green, S. F. Fung, V. M. Vasyliunas, D. L. Gallagher, and B. R. Sandel (2004), Plasmaspheric mass loss and refilling as a result of a magnetic storm, *J. Geophys. Res.*, *109*, A01202, doi:10.1029/2003JA009948.
- Sandel, B. R., et al. (1999), *The Extreme Ultraviolet Imager Investigation for the IMAGE Mission*, Springer, New York.
- Schulz, M. (1996), Eigenfrequencies of geomagnetic field lines and implications for plasma-density modeling, *J. Geophys. Res.*, *101*, 17,385.
- Southwood, D. J. (1974), Some features of field line resonances in the magnetosphere, *Planet. Space Sci.*, *22*, 482.
- Taylor, H. A., Jr., H. C. Brinton, and M. W. Pharo III (1958), Contraction of the plasmasphere during geomagnetically disturbed periods, *J. Geophys. Res.*, *73*, 961.

S. Abe, Venture Business Laboratory, Kyushu University, 6-10-1 Hakozaki Higashi-ku, Fukuoka, 812-8581, Japan. (abeshu@serc.kyushu-u.ac.jp)

D. G. Baishev and S. I. Solovyev, Institute of Cosmophysical Research and Aeronomy, Moscow, Russia.

J. Goldstein, Space Science and Engineering Division, Southwest Research Institute, San Antonio, TX, USA.

H. Kawano, Faculty of Science, Kyushu University, Fukuoka, Japan.

S. Ohtani, Johns Hopkins University Applied Physics Laboratory, Laurel, MD, USA.

K. Yumoto, Space Environment Research Center, Kyushu University, Fukuoka, Japan.